

Article

Explosion and Dynamic Transparency of Low-Density Structured Polymeric Targets Irradiated by a Long-Pulse KrF Laser

Vladimir D. Zvorykin ^{*}, Natalia G. Borisenko, Kirill S. Pervakov , Alexey V. Shutov and Nikolay N. Ustinovskii

P. N. Lebedev Physical Institute, Leninskii Prospekt, 53, 119991 Moscow, Russia; borisenkong@lebedev.ru (N.G.B.); pervakovks@lebedev.ru (K.S.P.); ash@lebedev.ru (A.V.S.); ustinovskiyinn@lebedev.ru (N.N.U.)

* Correspondence: zvorykin@sci.lebedev.ru

Abstract: The hydrodynamics of plasma formed in the interaction of 100 ns UV KrF laser pulses with foam targets with volume densities from 5 to 500 mg/cm³ was studied. Initial and dynamic transmittance at 248 nm wavelength were measured. At intensities of about 10¹² W/cm², the propagation rates of radiation through foam targets reached 80 km/s, while plasma stream velocities from both the front and rear sides of targets were approximately the same, ~ 75 km/s, which confirms a volumetric absorption of radiation within the target thickness and the explosive nature of the plasma formation and expansion.

Keywords: interaction of KrF laser with foams; foam-produced plasma expansion; propagation of laser radiation through foams



Citation: Zvorykin, V.D.; Borisenko, N.G.; Pervakov, K.S.; Shutov, A.V.; Ustinovskii, N.N. Explosion and Dynamic Transparency of Low-Density Structured Polymeric Targets Irradiated by a Long-Pulse KrF Laser. *Symmetry* **2023**, *15*, 1688. <https://doi.org/10.3390/sym15091688>

Academic Editor: Tomohiro Inagaki

Received: 8 August 2023

Revised: 30 August 2023

Accepted: 31 August 2023

Published: 2 September 2023



Copyright: © 2023 by the authors. Licensee MDPI, Basel, Switzerland. This article is an open access article distributed under the terms and conditions of the Creative Commons Attribution (CC BY) license (<https://creativecommons.org/licenses/by/4.0/>).

1. Introduction

The idea of Basov and Krokhin to fire with a laser thermonuclear (TN) reaction between deuterium and tritium (D–T) during a short time compared to the hydrodynamic expansion of heated plasma, i.e., to obtain the inertial confinement fusion (ICF) in the micro explosion [1], is currently under comprehensive investigation. It can either be performed by direct-drive irradiation of a shell target with TN fuel by laser light [2], or, in the indirect scheme, by converting laser radiation into X-rays in a cylindrical capsule with a target inside [3]. Now that the ignition of a TN reaction has been achieved in the indirect-drive by the NIF Nd: glass laser [4], it is quite obvious from a prolonged experimental run [5–8] that the main obstacle on the path to ignition are hydrodynamic instabilities. From initial perturbations caused by either target imperfections or X-ray irradiation asymmetry, they rapidly develop into the turbulent phase during shell acceleration, as well as its deceleration, before the target collapse.

In the direct-drive scheme, initial small-scale perturbations besides the roughness of the shell surface, are mainly caused by speckles that are typical for irradiation by a coherent light. A large-scale asymmetry arises, either because of a limited number of laser beams, even in the advanced ICF laser facilities (e.g., about 200 for the biggest ones NIF [9] and LMJ [10]), or because of energy imbalance between the beams. The latter originates from energy exchange in the course of nonlinear laser interaction with an under-dense outer plasma corona [11]. The small-scale hydrodynamic perturbations are seeded via “laser imprinting” at the very beginning of target irradiation, before the plasma corona is formed: light inhomogeneities are directly transformed into an inhomogeneous profile of the ablation front moving inward through the shell [12]. The growth of instabilities and their transition into turbulence lead to the mixing of the TN fuel and shell material, followed by temperature and density decrease in the target core, which results in a sharp fall of the TN reaction rate and prevents the TN fuel burning.

To create a uniform distribution of the laser radiation over a target surface, many optical methods have been developed (they are described, e.g., in the review [11]), such as

random phase plates, phased zone plates, and kinoform phase plates. In addition, optical smoothing was demonstrated by angular dispersion of frequency-modulated laser light and by induced spatial incoherence (ISI) produced by echelons. To reduce the effect of laser imprinting, in addition to optical methods, there are various hydrodynamic methods based on the creation of a plasma layer in front of the target, with a density gradient towards the target, before the arrival of the main heating pulse. Such absorbing plasma, with a density somewhat higher than the critical one, evens out the irradiation inhomogeneities due to transverse thermal diffusion [13]. It can be created by ionizing a gas [14] or a porous medium, e.g., a foam with a low-volume density placed in front of the plastic ablator by a low-energy prepulse [15,16]. A near-critical-density (NCD) preheated foam plasma can also be produced by X-ray radiation from a nearby laser–plasma source [17,18], or by using a thin (<1000 Å) layer of a high-Z material, which is deposited on the target surface or incorporated into the foam facing the laser [19–21]. In the latter case, laser-heated high-Z plasma effectively re-radiates in the soft X-ray range, causing uniform ablation of the target. As a result, the distance between the absorption zone of the laser radiation near the critical plasma density and the ablation front increases, which leads to smoothing of the laser imprint.

Laser–foam interaction, including the ionization dynamics of foams, have been studied experimentally and theoretically in many works, mostly with Nd: glass lasers at a wavelength of $\lambda = 1060$ nm, sometimes at second (2ω) or third (3ω) harmonics (see, for example, [22–38]). It is commonly assumed that foams are initially transparent for laser radiation and that plasma originates from the evaporation and ionization of pore septa. Meanwhile, compared with an Nd: glass laser, the KrF laser looks more attractive in the role of an ICF driver, and, especially, for the production of the Inertial Fusion Energy (IFE), as it can be scaled to the required sub-megajoule pulse energy, operate with an overall efficiency of up to 7% at rep-rate 5–10 Hz, and be arranged by a focal spot zooming synchronously with a target implosion [39,40]. As the KrF fundamental radiation UV wavelength of $\lambda = 248$ nm is one and a half times less than the 3ω Nd: glass laser, it has a number of important advantages in laser–target interaction: higher ablation pressure and efficiency of laser energy transfer into the kinetic energy of the imploding target, higher thresholds of laser–plasma instabilities (LPI) in the plasma corona, and, accordingly, a lower amount of harmful, fast “superthermal” electrons preheating the dense target core before the collapse. The effective echelon-free ISI smoothing of a broad-bandwidth radiation with a noncoherent master oscillator was implemented at the Nike KrF laser facility [41]. An overlapping of 44 noncoherent beams with a total energy about 1.7 kJ in 4 ns pulses produced on a planar target intensity of $I \sim 10^{14}$ W/cm², with the highest ever achieved uniformity and an rms deviation $\sim 0.15\%$, within the spot of 500–1000 μm . A stepwise laser pulse-form used in early experiments [42,43] and supposed for the ICF-scale target design [44] had a low-intensity “foot” of 3 to 5 ns in length with $I = 10^{12}–10^{13}$ W/cm², which sets the required compression adiabat of the imploding target. In such conditions, laser-imprinted perturbations were still observed for polystyrene (CH) targets with an rms roughness <30 Å, but hydrodynamic smoothing reduced them by an order of magnitude.

Among other foam applications, experiments at the five-beam Shenguang III 3ω Nd: glass laser facility could be mentioned [37], in which a homogenous, long-scale NCD plasma was produced by four laser beams with total energy 3.2 kJ in 1 ns pulses with an intensity of $I \approx 8 \times 10^{14}$ W/cm² from uniformly irradiated foam with a density of ~ 10 mg/cm³. Interaction of the fifth delayed beam at an intensity of $I \sim 10^{15}$ W/cm² with the plasma was investigated, which modeled the LPI development in the ICF-scale conditions. Thick NCD foam targets were used by Romsej et al. for direct laser acceleration (DLA) of electrons at a relativistic intensity of 10^{19} W/cm² in a homogeneous plasma channel of sub-mm length preformed by a nanosecond laser pulse with an intensity of $I \approx 5 \times 10^{13}$ W/cm² [45,46]. Long foam plasma gave a significant advantage in the DLA compared with a short-scale plasma produced in a conventional laser–foil interaction.

The present studies with low-density foam targets performed with a long-pulse GARPUN KrF laser at a relatively low peak intensity of $\sim 10^{12}$ W/cm² were motivated by our previous experiments [47,48] where, in a specific two-dimensional (2D) geometry, high-aspect-ratio capillary channels were obtained in semitransparent polymeric materials, e.g., polymethyl methacrylate (PMMA), and they revealed obvious features of the UV radiation waveguide. A direct electron acceleration in self-produced or preliminary drilled capillaries was observed up to a few hundred keV [49], which was associated with a longitudinal component of the electric field in a corrugated waveguide, which retarded the light in phase with electrons [50]. It is expected that the 2D hydrodynamics of low-density foam targets for a 100 ns laser pulse would be rather different from the case of 1D geometry typical for the most laser-foam interaction studies [22–38] carried out with ns-scale laser pulses. In addition, most plastic materials have a steep rise in absorbance around the KrF laser wavelength [48], which should decrease the plasma formation time for foams. Therefore, we believe that mm-scale plasma channels could be obtained with long KrF laser pulses.

2. Experimental Setup

2.1. GARPUN KrF Laser Description and Performance of Experiments

Two sets of experiments were performed at the GARPUN KrF laser facility with foam targets. Firstly, an initial foam transparency was measured at a low laser intensity of $I \leq 10^6$ W/cm² below the plasma formation threshold. After that, the dynamic transparency of foams was investigated in the intensity range of $I = (1–6) \times 10^{10}$ W/cm² when the targets evaporated during the action of the laser pulse. A discharge-pumped Lambda Physik EMG 150 TMS laser was used in these measurements, which generated pulses of asymmetric bell-like shape with a maximal energy of $E_{max} = 250$ mJ, a temporal width of $\tau = 20$ ns at FWHM, and a beam divergence of ~ 0.2 mrad. By using a step-wise diffraction attenuator DVA-22-250 (Inst. of Automation and Electrometry, Siberian Branch of RAS), the energy was varied in the range of $E = (0.01 \div 0.94) \times E_{max}$ before being focused by a lens with $F = 1$ m on the samples (see Figure 1). The energies of the incident and transmitted radiation were measured by PESO-SH-V2 calorimeters with a NOVA II display (Ophir Photonics Group, Israel), and the pulse shapes were measured by photodiodes (PD) Thorlabs DET10A and a TDS 2024 200 MHz (Tektronix Inc., USA) oscilloscope with ~ 2 ns temporal resolution. The radiation distribution in a focal plane was measured with a Spiricon SP620U profiler (Ophir Photonics), while a K8 glass plate was used to convert the UV laser light into green fluorescence [49]. The focal distribution had a Gaussian-like symmetric central part of 60 μ m diameter at the FWHM and broad low-intensity wings that originated from a temporal evolution of laser light in the unstable resonator cavity of the laser [49]. Readings from Calorimeter 1 and PD1 signals, together with the focal spot distribution, allowed the calculation of the peak values of energy density and intensity on the irradiated samples, while Calorimeter 2 and PD2 measured the energy and a pulse form of transmitted radiation.

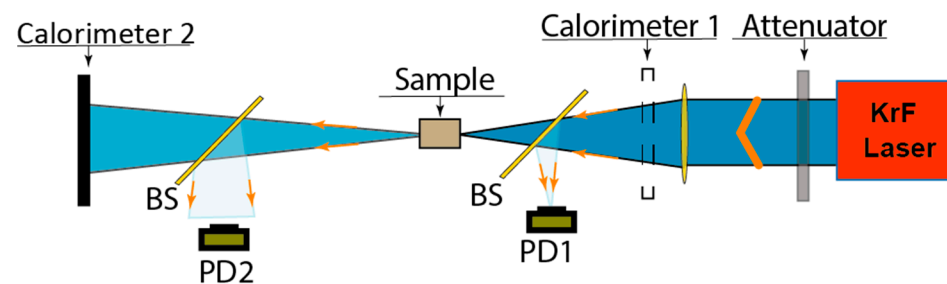


Figure 1. Layout of transmittance measurements.

The initial sample transparency was measured in the same scheme, but the focusing lens was replaced by a diaphragm with a diameter of 1 mm, which allowed us to probe small samples with a uniform intensity distribution quite below plasma formation.

The second set of experiments was carried out on a large-volume GARPUN KrF laser with a two-counter-side e-beam pumping. It was equipped with an unstable telescopic resonator (magnification parameter $M = 6$) and generated, in the injection-controlled operation mode, 100 J and 100 ns trapezoidal pulses with a rise front of 20 ns. An EMG 150 TMSO laser was used as a master oscillator, from which pulses were distributed between 4 laser-triggered switches in a high-voltage pulsed power supply of e-beam cold-cathode guns, while a small rest fraction was injected into the resonator cavity of the GARPUN laser, thus providing a quasi-steady divergence of output radiation $\sim 2 \times 10^{-4}$ (for other details, see [48]). A slightly convergent output laser beam with an initial cross section of $14 \times 18 \text{ cm}^2$ was directed into the vacuum chamber and focused by a spherical mirror with $F = 400 \text{ mm}$ in a spot of $150 \mu\text{m}$ diameter (at 0.1 level of the maximum), which contained 75% of the whole energy [47]. The peak intensity in the center of the focal spot was about 10^{12} W/cm^2 in the present experiments.

Various foam targets were placed in the vacuum chamber at the adjustable suspension. The layout of plasma imaging in visible light is shown in Figure 2a (see also [49]). A plasma plume was imaged with an objective, with $F = 210 \text{ mm}$, onto the intermediate plane, where an optical slit cut out a narrow strip oriented parallel to the incident laser beam. A time scanning of the strip was obtained by the “Agat” streak-camera with a time resolution of $\sim 100 \text{ ps}$. A “burn-through” time, the time it takes for laser radiation to penetrate through the tested target, was measured with an additional thick Al screen placed behind the target (Figure 2b). When the tested target became transparent, plasma was created on the screen, which allowed us to find the ablation front velocity inside the target. Preliminary target alignment on the streak camera screen was carried out in the “static mode” (without temporal scanning of the image) using a collimated probe beam produced by a telescope from an additional light source in the absence of a laser “shot”. By using a lens, an image from the camera screen was displayed on the profilometer.

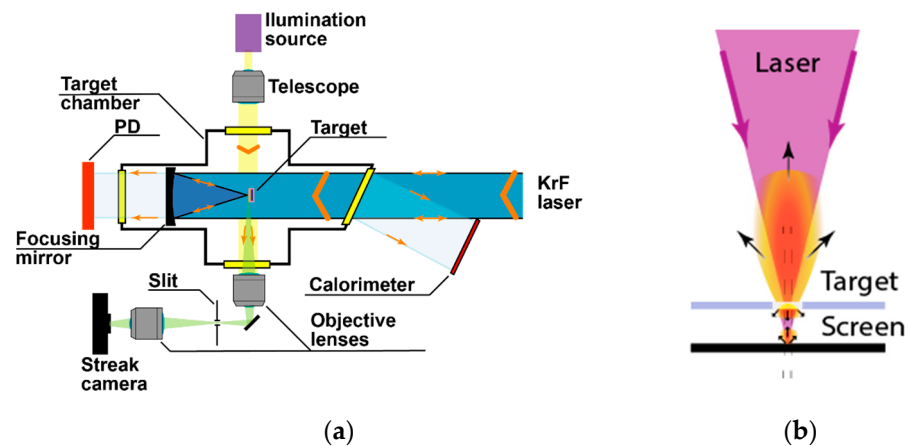


Figure 2. Optical scheme for (a) studying the laser–target interaction and (b) measuring the burn-through time of targets.

2.2. Foam Target Preparation

Structured polymer low-density materials (PLDM) based on super-crosslinked polymers have been manufactured for experiments in the GARPUN KrF laser facility using a technology developed in [51,52]. Linear polymers—polystyrene, poly-alpha-methylstyrene, polyacenaphthylene, polyvinyl naphthalene, polyvinylcarbazole, and oligomethylphenylsiloxane – were used as starting polymers for the production of PLDM with the elemental composition of C-H, C-H-Si-O, and C-H-N. High-molecular samples were synthesized by low-temperature cation polymerization. Super-crosslinked polymers in the form of organogels were obtained by crosslinking polymer macrochains in the Friedel–Crafts reaction in an organic solvent medium with chlorine-containing cross-agents, p-xylenedihloride and bis(chloromethyl)biphenyl. The synthesized polymer meshes have a rigid spatial structure,

since they contain repeatedly connected benzene rings. In such a polymer, short interstitial fragments form a volumetric molecular framework with nanoscale cavities—micropores. On the other hand, a structurally rigid molecular mesh is formed in a dilute polymer solution. As a result of drying, larger cavities are formed—mesopores and macropores. Due to such a special molecular architecture, the obtained materials have a developed pore system with a specific surface area of up to $1800 \text{ m}^2/\text{g}$ and a low volume density.

Detailed studies of the porous structure were carried out using the method of low-temperature adsorption of nitrogen at 77 K and carbon dioxide at 273 K with the NovaTouch apparatus (Quantachrome Corp., Boynton Beach, FL, USA). The main characteristics of the porous structure of the PLDM were determined—specific surface area, pore volume, parameters of the fractional composition of the pore system—surface, volume and size of pores, pore size distribution functions, etc. The density of the obtained materials was determined by hydrostatic weighing.

Several types of PLDM targets were selected for the present laser experiments. They differed in composition and manufacturing technology, as well as in volume density and shape (Figure 3). The highest density among them were targets made of CH polymer, $\rho = 150\text{--}500 \text{ mg}/\text{cm}^3$, made in the form of cylinders with a diameter of up to several millimeters (a). The lowest density, down to $\rho \sim 5 \text{ mg}/\text{cm}^3$, with a thickness l of hundreds of microns, had PLDM from CHO polymer (b). It was formed by drying the gel on a special copper hoop, and the thickness set the thickness of the foam target. The plasma glow in the direction perpendicular to the laser beam was registered through the slot made in the hoop. SiO_2 aerogel targets, obtained by the method of supercritical drying of a colloidal silica gel solution in methanol, had a volumetric density in the range $\rho = 100\text{--}150 \text{ mg}/\text{cm}^3$ and a different shape with a thickness of up to several millimeters (c, d).

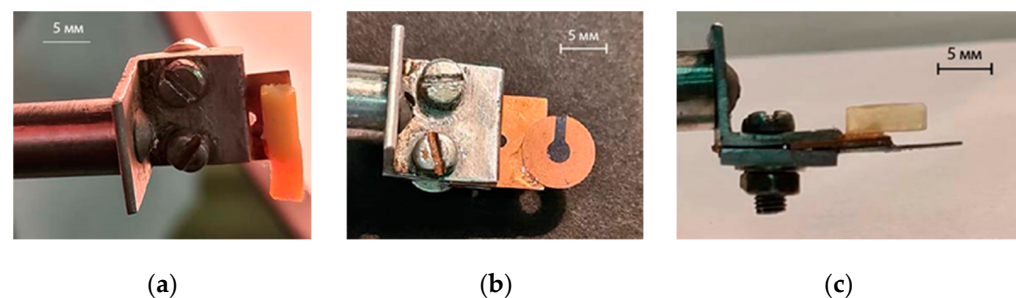


Figure 3. Photos of foam targets made of (a) CH polymer in the form of a cylinder, (b) CHO film on a hoop, and (c) SiO_2 aerogel in the form of a parallelepiped.

The PLDM targets were fixed in the interaction chamber at the suspension holder, and they were adjusted so that their frontal surfaces were in the focal plane of the focusing mirror. An additional screen for recording the burn-through time of the target was located a few millimeters behind a foam target (Figure 3c).

3. PLDM Transmittance

3.1. Initial PLDM Transmittance at 248 nm Wavelength

The initial transmittance of PLDM targets was measured at the wavelength of $\lambda = 248 \text{ nm}$ with a discharge-pumped KrF laser at low intensities of UV radiation, $I \leq 10^6 \text{ W}/\text{cm}^2$, quite below the threshold of target evaporation. An aperture of 1-mm cut out a collimated probe beam which passed through the sam-ples. Pulses of incident and transmitted radiation reflected by beam-splitters (BS) were registered by two PDs (Figure 1). With the help of a diffraction attenuator, the energy of the incident radiation could be varied by two orders of magnitude. Preliminarily PDs calibration, relative each other, was performed in the absence of a target. Within the measurement accuracy, the PLDM targets made of CH polymer completely absorbed UV radiation. The transmittance of the targets made of CHO foam with a thickness of $l \approx 150 \mu\text{m}$ and the SiO_2 aerogel

($l \approx 3$ mm) was $T_{low} = 0.15–0.20$ and $0.05–0.08$, respectively, and it did not depend on the incident intensity. For the given thicknesses of these targets, which differed by more than an order of magnitude, we found that SiO₂ aerogel has the lowest effective (taking into account scattering in matter) absorption coefficient of $\alpha = (1/l)\ln(1/T_{low}) \approx 10$ cm⁻¹ among the tested PLDM targets. In CHO foam, it was $\alpha \approx 10^2$ cm⁻¹.

3.2. Dynamic PLDM Transmittance during Thermal Explosion

A thin CH film with a thickness $l = 0.9$ μm and a density of $\rho \approx 1$ g/cm³ was chosen for comparison with the PLDM targets. Initially, it was fully opaque to UV laser radiation ($T_{low} \approx 0$), although its areal density, $\rho l \approx 10^{-4}$ g/cm², was comparable to that of thin CHO foams with $\rho l \sim 10^{-4}$ g/cm². PLDM targets made of CH polymer had a much lower areal density of $\rho l = 5 \times 10^{-2}–1.5 \times 10^{-1}$ g/cm². For SiO₂ aerogel, $\rho l = (3–5) \times 10^{-2}$ g/cm². Typical oscilloscope traces of incident and transmitted radiation, measured in the layout shown in Figure 1, are shown for different foams and intensities in Figure 4 and for CH film in Figure 5. It can be seen that transmitted radiation through the foams (PD2 signals) with a nonzero initial transmittance appears synchronously with the beginning of the laser pulse (PD1 signals), while the PD2 maximum is delayed by about 7 ns relative to the PD1 maximum. For opaque CH-films, PD2 signals start ~15 ns later than PD1, with the maximum delayed by ~15 ns. This means that, during the irradiation, the dynamic transmittance of both foams and the CH-film grew rapidly because of target evaporation and plasma enlightenment under expansion.

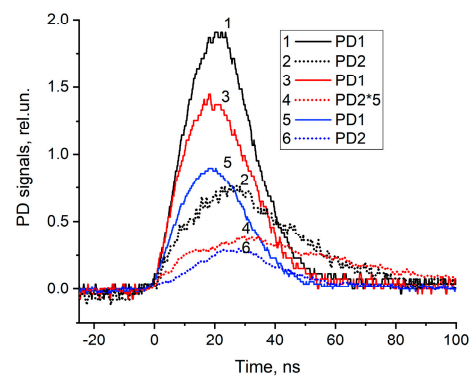


Figure 4. Oscilloscope traces of incident (PD1) and transmitted (PD2) radiation for different foams and peak intensities: (1, 2) CHO foam, $I = 6 \times 10^{10}$ W/cm²; (3, 4) SiO₂ aerogel, $I = 4.5 \times 10^{10}$ W/cm²; (5, 6) CHO foam, $I = 2.8 \times 10^{10}$ W/cm². The PD2 signal (4) is multiplied by 5.

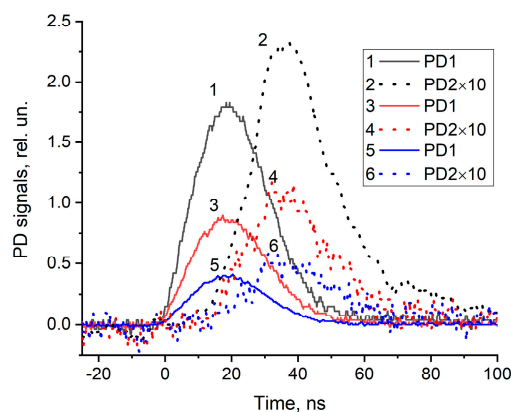


Figure 5. Oscilloscope traces of incident (PD1) and transmitted (PD2) radiation for CH-film at peak intensities: (1, 2) $I = 6 \times 10^{10}$ W/cm²; (3, 4) $I = 2.7 \times 10^{10}$ W/cm²; (5, 6) $I = 1.3 \times 10^{10}$ W/cm². All PD2 signals were multiplied by 10.

Figure 6 demonstrates a ratio of PD2 to PD1 signals for foams obtained from Figure 4. The same dependence for a CH film in Figure 7 was obtained from Figure 5.

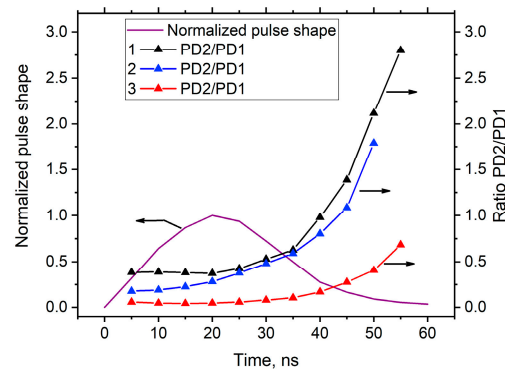


Figure 6. A normalized laser pulse shape and PD2/PD1 ratio obtained for (1) CHO foam, $I = 6 \times 10^{10} \text{ W/cm}^2$; (2) CHO foam, $I = 2.8 \times 10^{10} \text{ W/cm}^2$; (3) SiO_2 aerogel, $I = 4.5 \times 10^{10} \text{ W/cm}^2$.

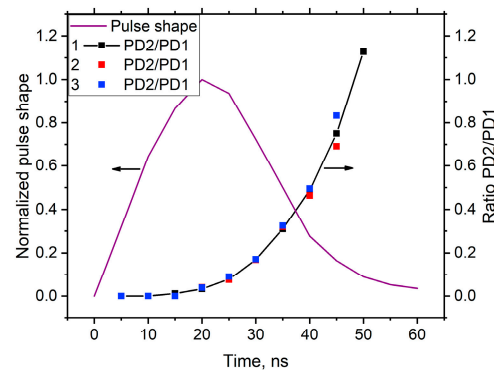


Figure 7. A normalized laser pulse shape and PD2/PD1 ratio obtained for CH films at (1) $I = 6 \times 10^{10}$; (2) $I = 2.7 \times 10^{10}$; (3) $I = 1.3 \times 10^{10} \text{ W/cm}^2$.

A dynamic foam transmittance, defined as a ratio of PD2/PD1 vs. time $T(t)$ and its initial values T_0 taken before $T(t)$ begins to grow, was measured. It depended on the individual foam properties and the foam's thickness. For thinner CHO foam (1), $T_0 \approx 0.38$, while, for the thicker one (3), $T_0 = 0.18\text{--}0.2$. The latter is in agreement with the low-intensity measurements T_{low} for the $150 \mu\text{m}$ foam (see Section 3.1). The SiO_2 aerogel had an initial transmittance of $T_0 = 0.04\text{--}0.05$, which was in agreement with a low-intensity value. A thermal target explosion and ionization was manifested by a rapid growth of the PD2/PD1 ratio. A similar PD2/PD1 growing behavior was observed for CH films, but it was less pronounced.

It is remarkable that, for CHO foams, the PD2/PD1 ratio overcame the maximum value $T = 1$, which assumes a fully transparent target for incident radiation. But, taking into account that the photodiode receiving area of $\sim 1 \text{ mm}^2$ in size was much lower compared to the laser beam cross section; the obtained PD2/PD1 value of 2.8 evidently indicated that a waveguide-like plasma channel was formed in the foam, because of which the laser pulse was redistributed and somewhat focused on PD2.

4. PLDM Hydrodynamics

A typical hydrodynamic picture of high-energy 100 ns pulse interaction with foam targets using the GARPUN laser is illustrated in Figure 8. At an irradiation intensity of $I \approx 10^{12} \text{ W/cm}^2$, the plasma produced from a CHO foam with a thickness of $l = 200 \mu\text{m}$ and a density of $\rho = 20 \text{ mg/cm}^3$ expanded from the front side of the target towards the incident radiation and from the back side in the laser beam direction with approximately

equal velocities of $v \approx 75$ km/s (a). This manifested a rapid volumetric absorption of radiation inside the foam that caused the explosive nature of the plasma formation. When the pulse energy E (and, accordingly, the intensity) was reduced by 4.8 times, the plasma expansion velocity decreased down to $v \approx 55$ km/s (b). This means that the dependence of plasma front velocity on laser energy is $v \propto E^{1/5}$, thus formally coinciding with Sedov–von Neumann–Taylor solution for a strong blast wave. Its radius R and velocity v scale as [53]:

$$R = \left(\frac{\alpha E}{\rho_0} \right)^{1/5} t^{2/5}, \quad v = \frac{2}{5} \left(\frac{\alpha E}{\rho_0} \right)^{1/5} t^{-3/5} \quad (1)$$

Here, E is the energy release, ρ_0 is the medium density, and α is the coefficient depending on the adiabatic index γ ; for $\gamma = 1.4$ in air, $\alpha \approx 1$.

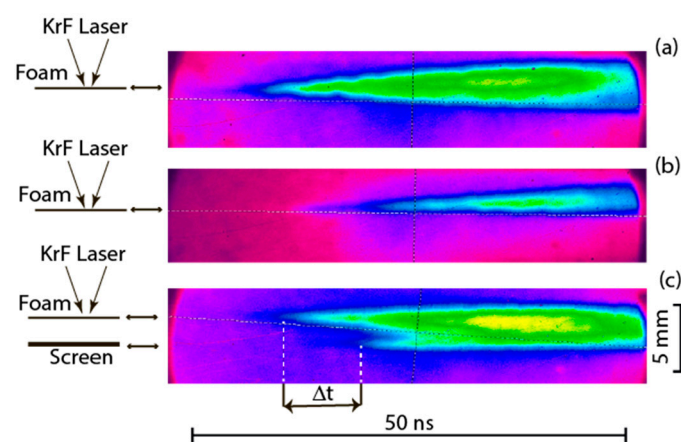


Figure 8. Streak images of CHO foam with density $\rho = 20$ mg/cm³, with different thicknesses l and peak irradiation intensities I : (a) $l = 200$ μm , $I \approx 10^{12}$ W/cm²; (b) $l = 200$ μm and $I \approx 0.21 \times 10^{12}$ W/cm²; (c) $l = 400$ μm and $I \approx 0.93 \times 10^{12}$ W/cm², with Al screen behind.

Formula (1) is exactly valid for a strong instantaneous point massless explosion. It was also used to estimate the energy load in the foam explosion produced by a nanosecond pulse [32]. In our case of a long 100 ns laser pulse, which was comparable with a hydrodynamic time scale, after a rapid foam explosion, the produced plasma cloud quickly became transparent to UV radiation, and only a small fraction of the laser energy was released in the foam.

However, a finite time of the foam explosion and a finite focal spot size resulted in a different $R(t)$ dependence (Figure 9) compared with Formula (1). It was only for the later time of $t \geq 35$ ns that the plasma blow-up velocity followed a relation of $R \propto t^{2/5}$. By this moment, the mass of the surrounding air became involved with the blast wave (for a residual pressure in the interaction chamber of ~ 0.1 Torr) and became comparable with the evaporated foam mass. An asymmetry between the foam expansion in the forward R_1 and backward R_2 directions was observed, probably originating from the distribution of absorbed radiation inside the foam.

Measurements of the burn-through time performed with CHO foam of $l = 400$ μm and $\rho = 20$ mg/cm³, and with an additional screen behind a target, as illustrated in Figure 8c, confirm very fast foam explosion and enlightenment. The CHO foam became transparent with a delay of $\Delta t \approx 10$ ns after the beginning of the laser pulse. In the case of a thick SiO₂ aerogel with $l = 2.5$ mm and $\rho = 100$ – 150 mg/cm³, the radiation passed through the plasma after ~ 30 ns. Thus, the measured burn-through rates are $v_b \approx 40$ km/s in CHO foam and $v_b \sim 80$ km/s in SiO₂ aerogel. These measurements correspond to effective mass ablation rates $\dot{m} = l/\rho v_b$: 8×10^4 and $\sim 10^6$ g/(cm²·s), respectively. A difference in \dot{m} by an order

of magnitude obviously originated from a tenfold difference in the CHO foam and SiO₂ aerogel absorption coefficients for laser radiation (see above, Section 3.2).

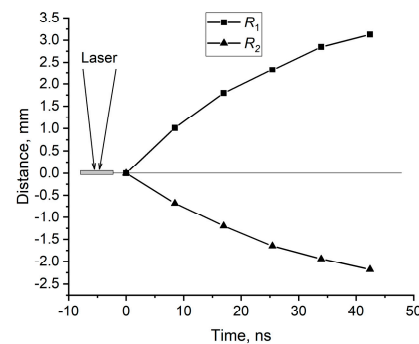


Figure 9. Time evolution of the blast wave distances from the front R_1 and from the back side R_2 of the CHO foam ($\rho = 20 \text{ mg/cm}^3$, $l = 200 \text{ }\mu\text{m}$, $I \approx 10^{12} \text{ W/cm}^2$).

Ablation rates \dot{m} in Al foil and graphite targets were measured in a similar layout earlier in the intensity range $I = (1-5) \times 10^{12} \text{ W/cm}^2$ [54]. Very high velocities were obtained for 100 ns pulses, which exceeded by an order of magnitude the measured ones for nanosecond pulses. They were mostly caused by a hydrodynamic radial displacement of matter by a megabar-scale ablation pressure. An approximation formula for \dot{m} was obtained:

$$\dot{m} = 2.6 \times 10^6 \left(I / 10^{13} \right)^{1/2}, \quad (2)$$

where \dot{m} is in $[\text{g}/(\text{cm}^2 \cdot \text{s})]$, and I is in $[\text{W}/\text{cm}^2]$.

In this regard, Al foils were used in the present experiments for comparison with the foam targets. For peak radiation intensity $I \approx 10^{12} \text{ W/cm}^2$, burn-through times of 10–50 ns have been measured for foils of $l = 20-110 \text{ }\mu\text{m}$ thicknesses (Figure 10), which corresponds to the burn-through rate in aluminum of $v_b \approx 2.2 \text{ km/s}$ and the effective mass ablation rate of $\dot{m} \approx 6 \times 10^5 \text{ g}/(\text{cm}^2 \cdot \text{s})$. These values coincide with our previous, above-mentioned measurements. Plasma expansion velocity towards the incident radiation was $v \approx 80 \text{ km/s}$, i.e., approximately the same as for the foam targets with a volume absorption.

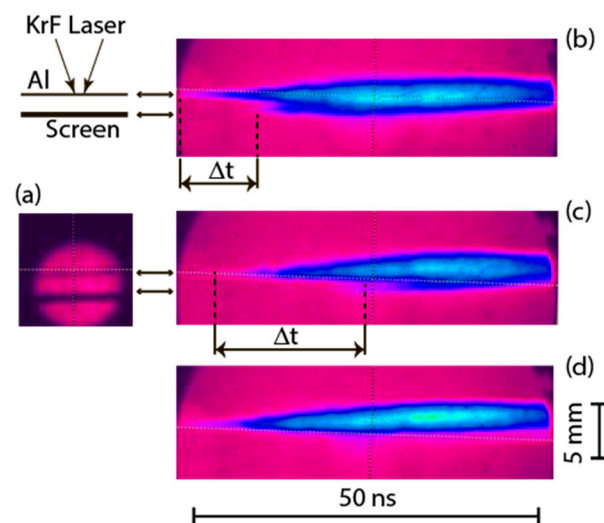


Figure 10. (a) Burn-through measurements for Al foils: (a) a static target image with an additional screen; streak images for $I \approx 10^{12} \text{ W/cm}^2$ and different thicknesses l (b) $l = 20$, (c) 50, and (d) 110 μm .

5. Summary

The present study filled a niche in the use of polymer low-density materials (PLDM) for the ICF applications and waveguide-like NCD plasma channel formation for electron acceleration, as most of the previous research has been carried out for laser wavelengths longer than 350 nm, whereas a KrF laser with a 248 nm UV wavelength is considered to be a promising driver for the ICF (see Section 1). Two PLDMs, namely, CHO foam with a volume density of $\rho = 5\text{--}20\text{ mg/cm}^3$ and SiO₂ aerogel with $\rho = 100\text{--}150\text{ mg/cm}^3$, were investigated with 20 ns laser pulses in regard to the initial (at a low laser intensity of $I \leq 10^6\text{ W/cm}^2$) and dynamic transmittance during foam plasma formation in the intensity range of $I = (1 - 6) \times 10^{10}\text{ W/cm}^2$. The latter measurements were compared with a dynamic transmittance of the initially opaque 0.9 μm CH film. Low-intensity absorption coefficients were found to be $\alpha \approx 10^2\text{ cm}^{-1}$ in CHO foam and $\alpha \approx 10^1\text{ cm}^{-1}$ in SiO₂ aerogel. An obvious feature of a waveguide-like plasma channel formation was revealed in an abnormal increase in PD laser light signals transmitted through the CHO foam.

An explosive character of plasma formation was demonstrated in the interaction of high-energy 100 ns laser pulses with CHO and SiO₂ PLDM. Plasma expansion velocity for CHO foam reached $v \approx 75\text{ km/s}$, and it was accompanied by a fast propagation of laser radiation through the foam thickness with the velocity of $v_b \approx 40\text{ km/s}$, which corresponded to effective mass ablation rate of $\dot{m} = 8 \times 10^4\text{ g/cm}^2\cdot\text{s}$. Even faster propagation, with $v_b \approx 80\text{ km/s}$ and $\dot{m} = 10^6\text{ g/cm}^2\cdot\text{s}$, was obtained in SiO₂ aerogel, and it was associated with an order of magnitude less absorption coefficient. On the other hand, close values of $\dot{m} = 6 \times 10^5\text{ g/(cm}^2\cdot\text{s)}$ for Al foil indicate the significance of 2D hydrodynamics in laser-foam interaction.

It was found that the experimental energy dependence $v \propto E^{\frac{1}{5}}$ satisfied the blast wave solution for a strong instantaneous point massless explosion, while the measured temporal dependence approached the theoretical one at $R \propto t^{\frac{2}{5}}$ when the mass of the residual air involved in the blast wave was comparable with the evaporated foam mass.

The obtained results for different kinds of PLDMs, differing in initial low-intensity transparency for UV radiation from a KrF laser and volume density, could serve as a suitable experimental benchmark for existing theoretical models of laser-foam interaction. The 2D hydrodynamic motion of matter, typical for a long 100 ns pulse, significantly increases the penetration rate of laser radiation through low-density foams. A few mm-scale waveguide-like plasma channels were produced in the foams that can be used for direct electron acceleration.

Author Contributions: Conceptualization, V.D.Z.; methodology, V.D.Z. and N.G.B.; PLDM target development, N.G.B. and K.S.P.; investigation, V.D.Z., N.N.U., A.V.S. and N.G.B.; writing—original draft preparation, V.D.Z.; writing—review and editing, N.N.U., A.V.S. and N.G.B. All authors have read and agreed to the published version of the manuscript.

Funding: This research was funded by the Ministry of Science and Higher Education of the Russian Federation in the framework of the research contract # 023-2019-0002.

Data Availability Statement: Upon a reasonable request.

Acknowledgments: The work was carried out under the auspices of the scientific program of the National Center for Physics and Mathematics in the frame of the State Contract No. H4c.241.4Д.23.1085. We are grateful to Veliev P.V. and Metreveli G.E. from P. N. Lebedev Physical Institute for their assistance with the experiments.

Conflicts of Interest: The authors declare no conflict of interest. Any other persons had no role in the design of the study; in the collection, analyses, or interpretation of data; in the writing of the manuscript; or in the decision to publish the results.

References

1. Basov, N.G.; Krokhin, O.N. Condition for heating up of a plasma by the radiation from an optical generator. *Sov. Phys. JETP* **1964**, *19*, 123–125.
2. Nuckolls, J.; Wood, L.; Thiessen, A.; Zimmerman, G. Laser compression of matter to super-high densities: Thermonuclear (CTR) applications. *Nature* **1972**, *239*, 139–142. [[CrossRef](#)]
3. Lindl, J. Development of the indirect drive approach to inertial confinement fusion and the target physics basis for ignition and gain. *Phys. Plasmas* **1995**, *2*, 3933–4024. [[CrossRef](#)]
4. National Ignition Facility Achieves Fusion Ignition. Available online: <https://llnl.gov/news/national-fusion-facility-achieves-ignition> (accessed on 14 December 2022); DOE National Laboratory Makes History by Achieving Fusion Ignition. Available online: <https://energy.gov/articles/doe-national-laboratory-makes-history-achieving-fusion-ignition> (accessed on 13 December 2022).
5. Pak, A.; Divol, L.; Casey, D.T.; Khan, S.F.; Kritcher, A.L.; Ralph, J.E.; Tommasini, R.; Trosseille, C.; Zylstra, A.B.; Baker, K.L.; et al. Dynamics and power balance of near unity target gain inertial confinement fusion implosions. *Phys. Rev. Lett.* **2023**, *131*, 065101. [[CrossRef](#)] [[PubMed](#)]
6. Lindl, J.; Landen, O.; Edwards, J.; Moses, E.; NIC Team. Review of the National Ignition Campaign 2009–2012. *Phys. Plasmas* **2014**, *21*, 020501. [[CrossRef](#)]
7. Montgomery, D.S. Two decades of progress in understanding and control of laser plasma instabilities in indirect drive inertial fusion. *Phys. Plasmas* **2016**, *23*, 055601. [[CrossRef](#)]
8. Robey, H.F.; Smalyuk, V.A.; Milovich, J.L.; Döppner, T.; Casey, D.T.; Baker, K.L.; Peterson, J.L.; Bachmann, B.; Hopkins, L.F.B.; Bond, E.; et al. Performance of indirectly driven capsule implosions on the National Ignition Facility using adiabat-shaping. *Phys. Plasmas* **2016**, *23*, 056303. [[CrossRef](#)]
9. Haynam, C.A.; Wegner, P.J.; Auerbach, J.M.; Bowers, M.W.; Dixit, S.N.; Erbert, G.V.; Heestand, G.M.; Henesian, M.A.; Hermann, M.R.; Jancaitis, K.S.; et al. National Ignition Facility laser performance status. *Appl. Opt.* **2007**, *46*, 3276–3303. [[CrossRef](#)]
10. Miquel, J.-L.; Lion, C.; Vivini, P. The Laser Mega-Joule: LMJ & PETAL status and program overview. *J. Phys. Conf. Ser.* **2016**, *688*, 012067. [[CrossRef](#)]
11. Craxton, R.S.; Anderson, K.S.; Boehly, T.R.; Goncharov, V.N.; Harding, D.R.; Knauer, J.P.; McCrory, R.L.; McKenty, P.W.; Meyerhofer, D.D.; Myatt, J.F.; et al. Direct-drive inertial confinement fusion: A review. *Phys. Plasmas* **2015**, *22*, 110501. [[CrossRef](#)]
12. Desselberger, M.; Afshar-rad, T.; Khattak, F.; Viana, S.; Willi, O. Nonuniformity imprint on the ablation surface of laser-irradiated targets. *Phys. Rev. Lett.* **1992**, *68*, 1539–1542. [[CrossRef](#)] [[PubMed](#)]
13. Emery, M.H.; Gardner, J.H.; Lehmborg, R.H.; Obenschain, S.P. Hydrodynamic target response to an induced spatial incoherence-smoothed laser beam. *Phys. Fluids B Plasma Phys.* **1991**, *3*, 2640–2651. [[CrossRef](#)]
14. Malka, V.; Faure, J.; Huller, S.; Tikhonchuk, V.T.; Weber, S.; Amiranoff, F. Enhanced spatiotemporal laser-beam smoothing in gas-jet plasmas. *Phys. Rev. Lett.* **2003**, *90*, 075002. [[CrossRef](#)]
15. Dunne, M.; Borghesi, M.; Iwase, A.; Jones, M.W.; Taylor, R.; Willi, O.; Gibson, R.; Goldman, S.R.; Mack, J.; Watt, R.G. Evaluation of a foam buffer target design for spatially uniform ablation of laser-irradiated plasmas. *Phys. Rev. Lett.* **1995**, *75*, 3858–3861. [[CrossRef](#)] [[PubMed](#)]
16. Metzler, N.; Velikovich, A.L.; Schmitt, A.J.; Gardner, J.H. Laser imprint reduction with a short shaping laser pulse incident upon a foam-plastic target. *Phys. Plasmas* **2002**, *9*, 5050–5058. [[CrossRef](#)]
17. Desselberger, M.; Jones, M.W.; Edwards, J.; Dunne, M.; Willi, O. Use of X-ray preheated foam layers to reduce beam structure imprint in laser-driven targets. *Phys. Rev. Lett.* **1995**, *74*, 2961–2964. [[CrossRef](#)]
18. Nishikino, M.; Shiraga, H.; Miyanaga, N.; Ohnishi, N.; Shigemori, K.; Fujioka, S.; Nakai, M.; Nishimura, H.; Azechi, H.; Mima, K.; et al. Imprint reduction in a plasma layer preformed with X-ray irradiation. *Phys. Plasmas* **2002**, *9*, 1381–1391. [[CrossRef](#)]
19. Hu, S.X.; Fiksel, G.; Goncharov, V.N.; Skupsky, S.; Meyerhofer, D.D.; Smalyuk, V.A. Mitigating laser imprint in direct-drive inertial confinement fusion implosions with high-Z dopants. *Phys. Rev. Lett.* **2012**, *108*, 195003. [[CrossRef](#)]
20. Karasik, M.; Weaver, J.L.; Aglitskiy, Y.; Oh, J.; Obenschain, S.P. Suppression of laser nonuniformity imprinting using a thin high-Z coating. *Phys. Rev. Lett.* **2015**, *114*, 085001. [[CrossRef](#)]
21. Aglitskiy, Y.; Zulick, C.; Oh, J.; Velikovich, A.L.; Schmitt, A.J.; Obenschain, S.P.; Karasik, M.; Weaver, J.L. Plasma hydrodynamic experiments on NRL Nike KrF laser. *High Energy Density Phys.* **2020**, *37*, 100866. [[CrossRef](#)]
22. Karasik, M.; Oh, J.; Obenschain, S.P.; Schmitt, A.J.; Aglitskiy, Y.; Stoeckl, C. Order-of-magnitude laser imprint reduction using pre-expanded high-Z coatings on targets driven by a third harmonic Nd: Glass laser. *Phys. Plasmas* **2021**, *28*, 032710. [[CrossRef](#)]
23. Koenig, M.; Benuzzi, A.; Philippe, F.; Batani, D.; Hall, T.; Grandjouan, N.; Nazarov, W. Equation of state data experiments for plastic foams using smoothed laser beams. *Phys. Plasmas* **1999**, *6*, 3296–3301. [[CrossRef](#)]
24. Batani, D.; Nazarov, W.; Hall, T.; Lower, T.; Koenig, M. Foam-induced smoothing studied through laser-driven shock waves. *Phys. Rev. E* **2000**, *62*, 8573–8582. [[CrossRef](#)]
25. Gus’Kov, S.; Gromov, A.; Merkul’Ev, Y.; Rozanov, V.; Nikishin, V.; Tishkin, V.; Zmitrenko, N.; Gavrilov, V.; Gol’Tsov, A.; Kondrashov, V.; et al. Nonequilibrium laser-produced plasma of volume-structured media and ICF applications. *Laser Part. Beams* **2000**, *18*, 1–10. [[CrossRef](#)]
26. Nishimura, H.; Shiraga, H.; Azechi, H.; Miyanaga, N.; Nakai, M.; Izumi, N.; Nishikino, M.; Heya, M.; Fujita, K.; Ochi, Y.; et al. Indirect–direct hybrid target experiments with the GEKKO XII laser. *Nucl. Fusion* **2000**, *40*, 547–556. [[CrossRef](#)]

27. Willi, O.; Barringer, L.; Bell, A.; Borghesi, M.; Davies, J.; Gaillard, R.; Iwase, A.; MacKinnon, A.; Malka, G.; Meyer, C.; et al. Inertial confinement fusion and fast ignitor studies. *Nucl. Fusion* **2000**, *40*, 537–545. [[CrossRef](#)]
28. Hall, T.; Batani, D.; Nazarov, W.; Koenig, M.; Bennuzzi, A. Recent advances in laser–plasma experiments using foams. *Laser Part. Beams* **2002**, *20*, 303–316. [[CrossRef](#)]
29. Limpouch, J.; Demchenko, N.N.; Gus’Kov, S.Y.; Kálal, M.; Kasperczuk, A.; Kondrashov, V.N.; Krouský, E.; Ek, K.M.; Pisarczyk, P.; Pisarczyk, T.; et al. Laser interactions with plastic foam-metallic foil layered targets. *Plasma Phys. Control. Fusion* **2004**, *46*, 1831–1841. [[CrossRef](#)]
30. Jiang, S.; Xu, Y.; Ding, Y.; Lai, D.; Zheng, Z.; Huang, Y.; Li, J.; Sun, K.; Hu, X.; Zhang, W.; et al. Experimental investigation of supersonic radiation propagation in low-density plastic and copper-doped foams. *Sci. China Ser. G Phys. Mech. Astron.* **2005**, *48*, 549–558. [[CrossRef](#)]
31. Tanabe, M.; Nishimura, H.; Ohnishi, N.; Fournier, K.B.; Fujioka, S.; Iwamae, A.; Hansen, S.B.; Nagai, K.; Girard, F.; Primout, M.; et al. Characterization of heat-wave propagation through laser-driven Ti-doped underdense plasma. *High Energy Density Phys.* **2010**, *6*, 89–94. [[CrossRef](#)]
32. Rozanov, V.B.; Barishpol’tsev, D.V.; Vergunova, G.A.; Demchenko, N.N.; Ivanov, E.M.; Aristova, E.N.; Zmitrenko, N.V.; Limpouch, I.; Ulschmidt, I. Interaction of laser radiation with a low-density structured absorber. *JETP* **2016**, *122*, 256–276. [[CrossRef](#)]
33. Cipriani, M.; Gus’Kov, S.Y.; De Angelis, R.; Consoli, F.; Rupasov, A.A.; Andreoli, P.; Cristofari, G.; Di Giorgio, G. Laser-driven hydrothermal wave speed in low-Z foam of overcritical density. *Phys. Plasmas* **2018**, *25*, 092704. [[CrossRef](#)]
34. Cipriani, M.; Gus’Kov, S.; De Angelis, R.; Consoli, F.; Rupasov, A.; Andreoli, P.; Cristofari, G.; Di Giorgio, G.; Ingenito, F. Laser-supported hydrothermal wave in low-dense porous substance. *Laser Part. Beams* **2018**, *36*, 121–128. [[CrossRef](#)]
35. Belyaev, M.A.; Berger, R.L.; Jones, O.S.; Langer, S.H.; Mariscal, D.A. Laser propagation in a subcritical foam: Ion and electron heating. *Phys. Plasmas* **2018**, *25*, 123109. [[CrossRef](#)]
36. Batani, K.; Aliverdiev, A.; Benocci, R.; Dezulian, R.; Amirova, A.; Krousky, E.; Pfeifer, M.; Skala, J.; Dudzak, R.; Nazarov, W.; et al. Shock dynamics and shock collision in foam layered targets. *High Power Laser Sci. Eng.* **2021**, *9*, e47. [[CrossRef](#)]
37. Roycroft, R.; Bradley, P.A.; McCary, E.; Bowers, B.; Smith, H.; Dyer, G.M.; Albright, B.J.; Blouin, S.; Hakel, P.; Quevedo, H.J.; et al. Experiments and simulations of isochorically heated warm dense carbon foam at the Texas Petawatt Laser. *Matter Radiat. Extrem.* **2021**, *6*, 014403. [[CrossRef](#)]
38. Tikhonchuk, V.T.; Gong, T.; Jourdain, N.; Renner, O.; Condamine, F.P.; Pan, K.Q.; Nazarov, W.; Hudec, L.; Limpouch, J.; Liska, R.; et al. Studies of laser-plasma interaction physics with low-density targets for direct-drive inertial confinement fusion on the Shenguang III prototype. *Matter Radiat. Extrem.* **2021**, *6*, 025902. [[CrossRef](#)]
39. Bodner, S.E.; Schmitt, A.J.; Sethian, J.D. Laser requirements for a laser fusion energy power plant. *High Power Laser Sci. Eng.* **2013**, *1*, 2–10. [[CrossRef](#)]
40. Obenschain, S.; Lehmberg, R.; Kehne, D.; Hegeler, F.; Wolford, M.; Sethian, J.; Weaver, J.; Karasik, M. High-energy krypton fluoride lasers for inertial fusion. *Appl. Opt.* **2015**, *34*, F103–F122. [[CrossRef](#)]
41. Obenschain, S.P.; Bodner, S.E.; Colombant, D.; Gerber, K.; Lehmberg, R.H.; McLean, E.A.; Mostovych, A.N.; Pronko, M.S.; Pawley, C.J.; Schmitt, A.J.; et al. The Nike KrF laser facility: Performance and initial target experiments. *Phys. Plasmas* **1996**, *3*, 2098–2107. [[CrossRef](#)]
42. Pawley, C.J.; Gerber, K.; Lehmberg, R.H.; McLean, E.A.; Mostovych, A.N.; Obenschain, S.P.; Sethian, J.D.; Serlin, V.; Stamper, J.A.; Sullivan, C.A.; et al. Measurements of laser-imprinted perturbations and Rayleigh–Taylor growth with the Nike KrF laser. *Phys. Plasmas* **1997**, *4*, 1969–1977. [[CrossRef](#)]
43. Obenschain, S.P.; Colombant, D.G.; Karasik, M.; Pawley, C.J.; Serlin, V.; Schmitt, A.J.; Weaver, J.L.; Gardner, J.H.; Phillips, L.; Aglitskiy, Y.; et al. Effects of thin high-Z layers on the hydrodynamics of laser-accelerated plastic targets. *Phys. Plasmas* **2002**, *9*, 2234–2243. [[CrossRef](#)]
44. Schmitt, A.J.; Bates, J.W.; Obenschain, S.P.; Zalesak, S.T.; Fyfe, D.E.; Betti, R. Direct drive fusion energy shock ignition designs for sub-MJ lasers. *Fusion Sci. Technol.* **2009**, *56*, 377–383. [[CrossRef](#)]
45. Rosmej, O.N.; E Andreev, N.; Zaechter, S.; Zahn, N.; Christ, P.; Borm, B.; Radon, T.; Sokolov, A.; Pugachev, L.P.; Khaghani, D.; et al. Interaction of relativistically intense laser pulses with long-scale near critical plasmas for optimization of laser-based sources of MeV electrons and gamma-rays. *New J. Phys.* **2019**, *21*, 043044. [[CrossRef](#)]
46. Rosmej, O.; Gyrdymov, M.; Günther, M.M.; E Andreev, N.; Tavana, P.M.; Neumayer, P.; Zähler, S.J.; Zahn, N.; Popov, V.S.; Borisenko, N.; et al. High-current laser-driven beams of relativistic electrons for high energy density research. *Plasma Phys. Control. Fusion* **2020**, *62*, 115024. [[CrossRef](#)]
47. Zvorykin, V.D.; Lebo, I.G.; Shutov, A.V.; Ustinovskii, N.N. Self-focusing of UV radiation in 1 mm scale plasma in a deep ablative crater produced by 100 ns, 1 GW KrF laser pulse in the context of ICF. *Matter Radiat. Extrem.* **2020**, *5*, 035401. [[CrossRef](#)]
48. Smetanin, I.V.; Shutov, A.V.; Ustinovskii, N.N.; Veliev, P.V.; Zvorykin, V.D. A new insight into high-aspect-ratio channel drilling in translucent dielectrics with a KrF laser for waveguide applications. *Materials* **2022**, *15*, 8347. [[CrossRef](#)] [[PubMed](#)]
49. Zvorykin, V.D.; Arlantsev, S.V.; Shutov, A.V.; Ustinovskii, N.N.; Veliev, P.V. Deep penetration of UV radiation into PMMA and electron acceleration in long plasma channels produced by 100 ns KrF laser pulses. *Symmetry* **2021**, *13*, 1883. [[CrossRef](#)]
50. Tadjima, T. High-energy laser plasma accelerators. *Laser Part. Beams* **1985**, *3*, 351–413. [[CrossRef](#)]
51. Pastukhov, A.V. Mesoporous polymer systems based on divinylbenzenecopolymers modified with linear rubbers. *Eur. Polymer J.* **2020**, *124*, 109480. [[CrossRef](#)]

52. Kovalev, A.I.; Pastukhov, A.V.; Tkachenko, E.S.; Klemenkova, Z.S.; Kuvshinov, I.R.; Khotina, I.A. Polyphenylenes with Phen-1,3,5-triyl branching moieties based on p-Diacetylbenzene: Synthesis and study of porosity and heat resistance. *Polym. Sci. Ser C.* **2020**, *62*, 205–213. [[CrossRef](#)]
53. Sedov, L.I. *Similarity and Dimensional Methods in Mechanics*; Academic Press: New York, NY, USA; London, UK, 1959; 363p.
54. Zvorykin, V.D.; Bakaev, V.G.; Lebo, I.G.; Sychugov, G.V. Hydrodynamics of plasma and shock waves generated by the high-power GARPUN KrF laser. *Laser Part. Beams* **2004**, *22*, 51–57. [[CrossRef](#)]

Disclaimer/Publisher's Note: The statements, opinions and data contained in all publications are solely those of the individual author(s) and contributor(s) and not of MDPI and/or the editor(s). MDPI and/or the editor(s) disclaim responsibility for any injury to people or property resulting from any ideas, methods, instructions or products referred to in the content.